

ApJ Letters; Received 2009 May 14; accepted 2009 June 2

Far-Infrared detection of neutral atomic oxygen toward the Horsehead Nebula¹

Javier R. Goicoechea

*Centro de Astrobiología (CSIC-INTA), Laboratorio de Astrofísica Molecular,
Carretera de Ajalvir, Km 4. Torrejón de Ardoz, 28850 Madrid, Spain.*

goicoechea@damir.iem.csic.es

Mathieu Compiègne

*Canadian Institute for Theoretical Astrophysics, University of Toronto,
60 St. George Street, Toronto, ON M5S 3H8, Canada*

compiagne@cita.utoronto.ca

and

Emilie Habart

Institut d'Astrophysique Spatiale, Université Paris-Sud, 91405 Orsay Cedex, France.

emilie.habart@ias.u-psud.fr

ABSTRACT

We present the first detection of neutral atomic oxygen ($^3P_1-^3P_2$ fine structure line at $\sim 63 \mu\text{m}$) toward the Horsehead photodissociation region (PDR). The cloud has been mapped with the *Spitzer Space Telescope* at far-IR (FIR) wavelengths using the Multiband Imaging Photometer for *Spitzer* (MIPS) in the spectral energy distribution (SED) mode. The [O I]63 μm line peaks at the illuminated edge of the cloud at $A_V \simeq 0.1-0.5$ (inward the gas becomes too cold and outward the gas density drops). The luminosity carried by the [O I]63 μm line represents a significant fraction of the total FIR dust luminosity ($I_{63}/I_{\text{FIR}} \simeq 4 \times 10^{-3}$). We

¹This work is based on observations made with the *Spitzer Space Telescope*, which is operated by the Jet Propulsion Laboratory, California Institute of Technology under a contract with NASA.

analyze the dust continuum emission and the *nonlocal* O I excitation and radiative transfer in detail. The observations are reproduced with a gas density of $n_{\text{H}} \simeq 10^4 \text{ cm}^{-3}$ and gas and dust temperatures of $T_k \simeq 100 \text{ K}$ and $T_d \simeq 30 \text{ K}$. We conclude that the determination of the O I 3P_J level populations and emergent line intensities at such “low” densities is a complex non-LTE problem. FIR radiative pumping, [O I]63 μm subthermal emission, [O I]145 μm suprathemal and even maser emission can occur and decrease the resulting [O I]63/145 intensity ratio. The *Herschel Space Observatory*, observing from ~ 55 to 672 μm , will allow us to exploit the diagnostic power of FIR fine structure lines with unprecedented resolution and sensitivity.

Subject headings: astrochemistry — infrared: ISM — ISM: atoms — ISM: clouds — line: formation — radiative transfer

1. Introduction

Oxygen is the most abundant heavy element in the Universe. Due to its relatively high ionization potential, far-ultraviolet (FUV) photons ($6 \text{ eV} < h\nu < 13.6 \text{ eV}$) do not ionize it and thus a large fraction of atomic oxygen can be expected in the photodissociated gas interface between the ionized and the molecular gas before chemical species such as CO, H₂O or OH reach high abundances. The absorption of FUV photons by dust grains leads to the ejection of photoelectrons that heat the gas (*e.g.*, Draine 1978) as well as to intense FIR dust continuum emission. The efficiency of this essential process can be estimated by comparing the luminosity of the main gas cooling lines (*e.g.*, the FIR fine structure lines of C II and O I) with the luminosity of the dust emission. Indeed, FIR lines from abundant gas reservoirs are key players in the energy balance of the regions they trace (from FUV illuminated interstellar clouds and protoplanetary disk surfaces to extragalactic starbursts).

The O I (3P_J) fine structure triplet system is formed by the 3P_2 (ground-state), the 3P_1 ($\Delta E_{12}/k=228 \text{ K}$) and the 3P_0 ($\Delta E_{01}/k=99 \text{ K}$) levels. Radiative transitions between the 3P_1 – 3P_2 and 3P_0 – 3P_1 states lead to the widespread [O I]63 and 145 μm line emission respectively. Observations and models of such lines are crucial diagnostics of a broad range of galactic and extragalactic environments (see Hollenbach & Tielens 1999 for a review).

In this Letter, we present the first detection of the [O I]63 μm line toward the Horsehead PDR ($d \sim 400 \text{ pc}$, edge-on), one of the most famous FUV-induced chemical laboratories in the sky. We analyze the FIR line and continuum emission without strong simplifying assumptions in the excitation and radiative transfer treatment.

2. Observations and Data reduction

The Horsehead nebula was observed with the Multiband Imaging Photometer for *Spitzer* (MIPS) as part of our “SPEC-PDR” program (ID:20281; Joblin et al. 2005) on 2006 April 3 using the spectral energy distribution mode (hereafter MIPS/SED). MIPS/SED provided the capability of obtaining low-resolution spectra ($R = 15 - 25$) in the FIR range ($\lambda = 55 - 97 \mu\text{m}$) using a slit spectrometer and the MIPS 70 Ge:Ga detector array. The slit size has two detector pixels in width ($\sim 20''$) and 12 pixels in length ($\sim 2'$). A reflective grating provides a spectral dispersion of $1.7 \mu\text{m pixel}^{-1}$. We used the “spectral mapping” mode and covered the Horsehead with 14 pointings shifted by half the slit width in the direction perpendicular to the slit length. The exposure time was 10s per pointing. The “chop distance” for the OFF positions was set to $+3'$ for each pointing. Both ON- and OFF-source areas are shown in Fig. 1a.

We subtract the average OFF-source spectrum to every ON-source spectra. We first retrieved the BCD data (ver. s16.1.0) that we proceed with the *mosaic-sed.pl* script of MOPEX¹ to obtain the post-BCD level data (in intensity units of MJy sr^{-1}). We apply a flat correction to the spatial dimension on the detector (*i.e.* detector columns relative gain correction) at the BCD level. We compute the flat response of the detector columns using the OFF positions. We have developed a pipeline that builds spectral cubes (two spatial dimensions and one spectral dimension) from the Post-BCD data. We work in the assumption that no spatial information is available in the slit width. Thus, the N_λ rows of the detector can be seen as images of the sky through the slit for N_λ sampled wavelengths between 55 and $97 \mu\text{m}$. For each wavelength, this image of the slit is reprojected into a $N_\alpha \times N_\delta$ spatial grid of the sky. The final cube then has $N_\alpha \times N_\delta \times N_\lambda$ pixels. The pixel size of the spatial grid is half of each detector pixel field-of-view, PFOV ($9.8''/2 = 4.9''$).

Nevertheless, due to dispersion, the light that falls on a pixel comes from the entire slit width, that is two times the pixel size, so that the PFOV is rather $9.8'' \times 19.6''$. This leads to an overestimation of the intensity of a factor 2 that we take into account here. For extended sources, one also has to correct for the effect of the aperture used for the photometric calibration with point sources. We then divide the intensity by the 5 pixels aperture correction function (see MIPS Data Handbook). The photometry of the resulting spectral cubes (for all sources in our program) were checked by cross-calibrating them with MIPS 70 data when available. It appears that the MIPS/SED gain is 30% higher than the MIPS 70 one. On the basis that the photometer calibration is more reliable, we apply this 30% correction to our MIPS/SED data and use the MIPS 70 absolute calibration uncertainty of 7%.

¹<http://ssc.spitzer.caltech.edu/postbcd/mopex.html>

3. Observational Results

Figure 1a shows the ON– and OFF–source areas of our *Spitzer* observations plotted over the polycyclic aromatic hydrocarbon (PAH) mid–IR emission toward the Horsehead (Abergel et al. 2003). The PAH band emission traces the FUV illuminated edge of the cloud (Compiègne et al. 2007, 2008; Goicoechea et al. 2009). MIPS spectra averaged over the ON and OFF areas are shown as green and blue histograms (Fig. 1b). The ON–OFF subtracted spectrum is shown as a black histogram. The [O I]63 μ m line is not present in the OFF spectrum, and therefore, the extended line emission can fully be attributed to the cloud.

In order to have an approximate view of the spatial location of the oxygen emission, Fig. 1c displays the [O I]63 μ m line intensity measured in each pixel of the data cube (gray scale). The *ortho*-H₂ $v=0-0$ $S(1)$ pure rotational line emission at ~ 17 μ m, delineating the edge of the PDR, is shown as white contours. Overall, the [O I] emission peaks in the warm cloud layers (where H₂ and PAH emission are also bright) directly exposed to the FUV radiation from σ Ori O9.5V star. Although the excitation requirements of the *ortho*-H₂ $v=0-0$ $S(1)$ ($E_u/k \simeq 1015$ K) and [O I]63 μ m ($E_u/k \simeq 228$ K) lines are different, the apparent shift between both line emission peaks in Fig. 1c may be marginal since MIPS/SED astrometry is not better than $\sim 5''$. Besides, cloud inclination variations (relative to the line of sight) from north to south, and thus differential line opacity effects, likely explain the brighter [O I]63 μ m emission observed toward the north of the filament.

The [O I]63 μ m line intensity toward the emission peak, as measured over the $\sim 15''$ full width at half maximum (FWHM) angular resolution of MIPS at 63 μ m (circle on Fig. 1c), is $I_{63} = (1.04 \pm 0.14) \times 10^{-7}$ W m⁻² sr⁻¹ (~ 4 times brighter than the H₂ $v=1-0$ $S(1)$ fluorescent emission at 2.12 μ m; see Habart et al. 2005). The resulting MIPS spectrum is shown in Fig. 1b as “PEAK”. The [O I]63 μ m line is detected at a 10σ level. The FIR thermal emission of dust raises from ~ 155 MJy sr⁻¹ (at ~ 55 μ m) to ~ 325 MJy sr⁻¹ (at ~ 85 μ m). The continuum peaks at longer wavelengths and thus the temperature of the grains emitting in the FIR (T_d) cannot be high ($T_d \lesssim 35$ K), lower than the expected gas temperature (T_k). Apart from this [O I]63 μ m bright emission toward the cloud edge, the MIPS data show a fainter level of widespread emission (~ 4 times weaker) likely arising from the more diffuse cloud envelope, or halo, illuminated by the ambient FUV radiation field.

4. Discussion

4.1. Physical conditions in the Horsehead PDR

In order to guide our interpretation of the [O I]63 μ m line toward the PEAK, Fig. 2 (*left*) shows the output of a photochemical model (Le Petit et al. 2006; Goicoechea & Le Bourlot 2007) adapted to the steep density gradient, $n_{\text{H}} \sim r^{-3}$ (Habart et al. 2005, Goicoechea et al. 2009) and FUV illumination conditions in the Horsehead edge ($G_0 \simeq 100$, where G_0 is the FUV flux in Habing units of the local interstellar value). We adopt an elemental oxygen abundance of 3×10^{-4} relative to H nuclei (Savage & Sembach 1996). Taking into account that the gas temperature rapidly decreases from the low density PDR ($T_k \simeq 100$ K; see also Pety et al. 2005; Habart et al. 2009) to the denser and shielded inner layers ($T_k \lesssim 20$ K; Pety et al. 2007), we predict that the [O I]63 μ m emission peak should occur at the surface of the molecular cloud between $A_V \simeq 0.1$ and 0.5. Due to the relatively low FUV radiation field impinging the cloud, dust grains are not expected to attain large temperatures ($T_d \lesssim 30$ K). However, H₂ photodissociation is still important in the cloud edge and a significant fraction of hydrogen is predicted to reside in atomic form in the same layers where [O I]63 μ m is bright. At extinction depths greater than $A_V \sim 1.5$, carbon monoxide starts to be protected against photodissociation and the gas temperature falls sharply. The formation of CO (and other O-rich gas and ice species) decreases the abundance of atomic oxygen inward.

4.2. Nonlocal and Non-LTE Modeling

Observations of the [O I]63 μ m line and FIR continuum emission constrain the mean gas density and both the dust and gas temperatures toward the PDR. In this work, we use a *nonlocal* and non-LTE code that treats both the line and continuum radiative transfer and includes the radiative pumping of O I levels by absorption of FIR dust photons (see the Appendix in Goicoechea et al. 2006). Almost all studies solving the excitation of atomic fine structure levels simplify the problem by assuming a *local* treatment of the excitation calculation: *LVG* or single-zone escape probability methods (*e.g.*, Röllig et al. 2007), where the source function (the line emissivity/absorption ratio) is assumed to be constant, and the radiative coupling between different cloud positions is neglected. The effects of dust opacity are also generally omitted (González García et al. 2008). Their applications to the interpretation of [O I]63,145 μ m lines have been widely used by a number of authors in the past (*e.g.*, Tielens & Hollenbach 1985; van Dishoeck & Black 1986; Spaans et al. 1994; Poglitsch et al. 1995; Kaufman et al. 1999; Vastel et al. 2001; Liseau et al. 1999, 2006). Nevertheless, Elitzur & Asensio-Ramos (2006) recently compared the exact solutions provided by their

nonlocal method with those given by the *local* approximation and concluded that, for gas densities around 10^3 – 10^4 cm^{-3} , the error in the predicted [O I]63/145 line intensity ratio can be significant (*i.e.*, comparable with the variation range of the ratio for different temperatures and densities). Indeed, these are the densities expected in the outer layers of the Horsehead nebula, *i.e.*, below the critical densities of O I fine structure transitions ($n_{\text{cr}} \simeq 5 \times 10^5$ cm^{-3} for O I (3P_1 – 3P_2)–H₂ collisional² de-excitation). Under these conditions, the determination of the 3P_J level populations is a non-trivial problem and radiative and opacity effects (FIR pumping and line-trapping) can play a role. Besides, the [O I]63 μm line becomes optically thick ($\tau_{63} > 1$) for low column densities, $N(\text{O I}) \gtrsim 10^{17}$ cm^{-2} , and the [O I]145 μm line can be suprathermal ($T_{\text{ex}} > T_k$) or even inverted ($T_{\text{ex}} < 0$) and the emission amplified ($\tau_{145} < 0$) by the maser effect (see also Liseau et al. 2006; Elitzur & Asensio–Ramos 2006).

4.3. FIR dust continuum emission

In order to constrain the dust temperature, the FIR dust luminosity and obtain an approximated value for the gas density in the [O I]63 μm emitting region, we have first modeled the observed SED toward the PEAK position. We explicitly solve the continuum radiative transfer problem by taking a dust opacity $\tau_d(\lambda)$ proportional to $\kappa_{100}(100/\lambda)^\beta$, where κ_{100} is the dust opacity at 100 μm (per gas+dust mass column density) and β is the dust spectral index. Assuming a line-of-sight depth of 0.1 pc (uncertain within a factor of ~ 2 , see constraints by Habart et al. 2005), the best models of the continuum shape and absolute intensity level are obtained for $T_d \simeq 30$ K (in agreement with the PDR model prediction) and $n_{\text{H}} = n(\text{H}) + 2n(\text{H}_2) \simeq 10^4$ cm^{-3} (with $\beta \simeq 1.4$ and $\kappa_{100} \simeq 0.25$ cm^2 g^{-1} ; *e.g.*, Li & Draine 2001). Integrating the resulting continuum intensity distribution from 40 to 500 μm we obtain $I_{\text{FIR}} = 2.5 \times 10^{-5}$ W m^{-2} sr^{-1} . The dust model is shown in Fig. 1b (red dashed curve). We determine that the line-of-sight extinction depth toward the PEAK is $A_V \simeq 1.5$, consistent with the expected values of a cloud edge. The FIR dust continuum toward the region of bright [O I], H₂, and PAH emission is optically thin, with $\tau_d(63) \simeq 2 \times 10^{-3}$.

²The collisional rate coefficients (γ_{ij}) used in this work are: O I collisions with *ortho/para*-H₂ from Jaquet et al. (1992): note that for low energies ($T_k \lesssim 300$ – 400 K), the γ_{02} and γ_{12} rates are slightly higher (*e.g.*, by $\lesssim 10\%$ at 100 K) when *para*-H₂ is the perturber. Otherwise, rate coefficients are slightly higher for *ortho*-H₂ collisions; O I–H collisions from Abrahamsson et al. (2007): at 100 K these excitation rate coefficients are a factor of ~ 4 larger than those by Launay & Roueff (1977); O I–He collisions from Monteiro & Flower (1987); O I– e^- collisions from Bell et al. (1998) and O I– p^+ collisions from Chambaud et al. (1980).

4.4. O I excitation and radiative transfer

After modeling the FIR radiation field in the PDR we now solve the O I 3P_J populations adding radiative pumping by FIR dust photons. We include collisional rate coefficients² ($\text{cm}^3 \text{s}^{-1}$) of atomic oxygen with *ortho*- and *para*-H₂, H, He, electrons, and protons. H₂ and H collisions dominate, but it is important to include their rates (s^{-1}) with the most realistic H and H₂ density contributions. Note that, for example, $^3P_1 - ^3P_0$ collisional excitation can be neglected (to first order) if only O I–H₂ collisions apply (Monteiro & Flower 1987), but it does contribute if collisions with H are included (Abrahamsson et al. 2007). We adopt an *ortho*-to-*para*-H₂ ratio² (OTP) of 3, although, at the T_k and n_{H} considered in this work, our results do not change by taking an OTP of 1 ([O I] lines become $\sim 2\%$ brighter).

Figure 2 (right) displays a grid of *nonlocal* models showing the emergent I_{63} intensity as a function of $N(\text{O I})$ column density. The lower panel shows the predicted I_{63} for $T_k=100 \text{ K}$ (*i.e.*, roughly the gas temperature in the outermost cloud layers) and varying H₂ densities. Guided by our PDR model (Figure 2 (left)), and in order to modify only one physical parameter in the grid, we take a fixed $n(\text{H})$ density of 10^3 cm^{-3} and a high ionization fraction: $n(e^-)/n_{\text{H}}=10^{-4}$ (see Goicoechea et al. 2009). Our calculations include thermal, turbulent, and opacity line broadening with a turbulent velocity dispersion of $\sigma=0.225 \text{ km s}^{-1}$ (FWHM= $2.355 \times \sigma$). This value is inferred from heterodyne interferometric observations of the HCO radical toward the PDR (Gerin et al. 2009). The shaded regions show the observed [O I]63 μm line intensity toward the PEAK position. For a line-of-sight depth of 0.1 pc and taking O I/H $\simeq 3 \times 10^{-4}$ in the PDR (most oxygen in atomic form), our observations are reproduced with $n(\text{H}_2)\simeq 5 \times 10^3 \text{ cm}^{-3}$ (consistent with the dust model) and $N(\text{O I})\simeq 8.5 \times 10^{17} \text{ cm}^{-2}$ (best model shown in Figure 1 (b)). The [O I]63 μm opacity at line center is $\tau_{63}\simeq 6$ (due to saturation the width of the line profile is opacity broadened, FWHM $\sim 1.3 \text{ km s}^{-1}$, *i.e.*, broader than the linewidth of an optically thin line affected only by turbulent and thermal dispersion). The predicted [O I]63/145 line intensity ratio is $\simeq 15$. The required H₂ density has to be multiplied (divided) by ~ 4 if the gas temperature is a factor of 2 lower (higher); line opacities and [O I]63/145 intensity ratios change accordingly. Future observations of both [O I]63,145 μm lines will help to better constrain the density and the atomic oxygen abundance gradient.

For $T_k=100 \text{ K}$, the [O I]63 μm line emission is subthermal ($T_{ex} < T_k$) which means that the 3P_1 level (n_1) is much less populated than in LTE (*i.e.*, $\frac{n_1}{n_2} \ll \frac{3}{5} e^{-\frac{228}{100}} \simeq \frac{1}{16}$). In fact we find that the $^3P_0 - ^3P_1$ transition at 145 μm is suprathermal (with $\frac{n_0}{n_1} \simeq \frac{1}{3} > \frac{1}{3} e^{-\frac{99}{100}} \simeq \frac{1}{8}$). This effect is produced by the larger radiative life time of the upper 3P_0 level compared to the lower 3P_1 level (by a factor of ~ 5). Even more, the lack of significant $^3P_0 - ^3P_1$ collisional de-excitation for O I–H₂ collisions (neglecting those with H) can invert the level populations

($\frac{n_0}{n_1} > \frac{1}{3}$) leading to a [O I]145 μm maser line emission. High temperatures ($T_k \gtrsim 100$ K for a pure H_2 gas and $T_k \gtrsim 300$ K for a pure H gas) together with relatively low τ_{63} opacities (or $n_{\text{H}} < 10^5 \text{ cm}^{-3}$) are required to obtain the level inversion, otherwise line-trapping in the [O I]63 μm line increases the upper 3P_1 level population again. At such “low” gas densities ($n_{\text{H}} < n_{\text{cr}}$) the *local* treatment of O I excitation overestimates (underestimates) the n_1 (n_0) level populations, leading to stronger (weaker) [O I]63 μm (145 μm) emission as long as $\tau_{63} \gtrsim 1$. The error made increases with $N(\text{O I})$ (see Elitzur & Asensio-Ramos 2006).

The FIR continuum toward the Horsehead is optically thin and radiative pumping does not play a significant role in the O I excitation (it reduces I_{63} by $\sim 1\%$). However, in more extreme sources (with opaque continuum emission), FIR pumping can reduce the T_{ex} of the O I 3P_1 - 3P_2 transition ($T_{\text{ex}} \rightarrow T_d$) and increase the n_0/n_1 level population ratio. For the physical conditions treated here, the [O I]63/145 ratio decreases by a factor of ~ 2 if the dust emission becomes optically thick at 63 μm . Overall, neglecting FIR pumping and using *local* approximations for the O I excitation overestimates the [O I]63/145 ratio.

4.5. Cooling rate and photoelectric heating efficiency

Once the non-LTE level populations have been accurately computed, one can determine the appropriate [O I]63 μm cooling rate per volume unit, $\Lambda_{63} = h\nu_{12} (n_2 C_{21} - n_1 C_{12})$ (where C_{ij} are the collisional excitation and de-excitation rates in s^{-1}). This relation takes into account that only line photons following collisional excitation and escaping the cloud are responsible of the gas cooling. We compute $\Lambda_{63} \simeq 5 \times 10^{-21} \text{ erg s}^{-1} \text{ cm}^{-3}$ toward the PEAK position.

Our observations and models are consistent with the [O I]63 μm line arising from the outer layers ($A_V \simeq 0.1$ and 0.5) of the Horsehead PDR ($G_0 \simeq 100$ and $n_{\text{H}} \simeq 10^4 \text{ cm}^{-3}$) where the gas is warm ($\simeq 100$ K) and not all available hydrogen has converted into H_2 yet. Together with available [C II]158 μm observations ($I_{158} \simeq (1-3) \times 10^{-7} \text{ W m}^{-2} \text{ sr}^{-1}$, from KAO at $\sim 55''$ resolution; Zhou et al. 1993), we find that the luminosity of the [C II]158 μm + [O I]63 μm lines represents $\sim 1\%$ - 2% of the total FIR dust luminosity. This fraction corresponds to a high efficiency of the photoelectric heating mechanism. In fact, due to the relatively low FUV field but moderate gas density in the PDR, the Horsehead is a good source to investigate the grain populations that efficiently transform the incident FUV field into gas heating.

Herschel will allow us to map almost all relevant FIR cooling lines at much higher spectral and angular resolutions. Together with appropriate models of their excitation, it will then be possible to study the energy balance of interstellar clouds in greater detail.

We thank the SPECPRD team for their contribution to the project, A. Noriega-Crespo and R. Paladini for valuable discussions on MIPS/SED data reduction and M. Gerin and the referee for helpful comments on the manuscript. JRG was supported by a *Ramón y Cajal* research contract from the Spanish MICINN and co-financed by the European Social Fund.

REFERENCES

- Abergel, A., Teyssier, D., Bernard, J. P et al. 2003, A&A, 410, 577
- Abrahamsson, E., Krems, R.V. & Dalgarno, A. 2007, ApJ, 654, 1171
- Bell, K.L., Berrington, K.A., Thomas, M.R.J. 1998, MNRAS, 293, L83
- Chambaud, G. et al. 1980, J.Phys.B, 13, 4205
- Compiègne M. et al. 2007, A&A, 471, 205
- Compiègne M. et al. 2008, A&A, 491, 797
- Draine, B. T. 1978, ApJS, 36, 95
- Elitzur, M. & Asensio-Ramos, A. 2006, MNRAS, 365, 779
- Gerin, M., Goicoechea, J.R., Pety, J., & Hily-Blant, P. 2009, A&A, 494, 977
- Goicoechea, J. R. & Le Bourlot, J. 2007, A&A, 467, 1
- Goicoechea, J. R. et al. 2006, A&A, 456, 565
- Goicoechea, J. R. et al. 2009, A&A, 498, 771
- González García, M., Le Bourlot, J., Le Petit, F. & Roueff, E. 2008, A&A, 485, 127
- Habart, E., Abergel, A., Walmsley, C. M., Teyssier, D. & Pety, J. 2005, A&A, 437, 177
- Habart, E., Abergel A., Boulanger F. et al. 2009, A&A, submitted.
- Hollenbach, D.J. & Tielens, A.G.G.M. 1999, Rev.Mod.Phys. 71, 173
- Jaquet, R., Staemmler, V., Smith, M. D. & Flower, D. R. 1992, J. Phys. B, vol. 25, 285
- Joblin, C., Abergel, A., Bernard, J.-P. et al. 2005, *sptz.prop20281*
- Kaufman, M.J., Wolfire, M.G., Hollenbach, D.J., Luhman, M.L. 1999, ApJ, 527, 795

- Launay, J. M. & Roueff, E. 1977, *A&A*, 56, 289
- Le Petit, F., Nehmé, C, Le Bourlot, J. & Roueff, E. 2006, *ApJS*, 64, 506
- Li, A. & Draine, B. T. 2001, *ApJ*, 554, 778
- Liseau, R. et al. 1999, *A&A*, 344, 342
- Liseau, R., Justtanont, K. & Tielens, A.G.G.M. 2006, *A&A*, 446, 561
- Monteiro, T. S. & Flower, D. R. 1987, *MNRAS*, 228, 101
- Pety, J., Goicoechea, J. R., Hily-Blant, P., Gerin, M. & Teyssier, D. 2007, *A&A*, 464, L41
- Pety, J., et al. 2005, *A&A*, 435, 885
- Poglitsch, A., Krabbe, A., Madden, S.C. et al. 1995, *ApJ*, 454, 293
- Röllig, M., Abel, N. P., Bell, T. et al. 2007, *A&A*, 467, 187
- Savage, B.D. & Sembach, K.R. 1996, *ARA&A*, 34, 279
- Spaans, M., Tielens, A.G.G.M., van Dishoeck, E.F. & Bakes, E.L.O. 1994, *ApJ*, 437, 270
- Tielens, A.G.G.M. & Hollenbach, D.J. 1985, *ApJ*, 291, 722
- van Dishoeck, E. F. & Black, J. H. 1986, *ApJS*, 62, 109
- Vastel, C., Spaans, M., Ceccarelli, C., Tielens, A. G. G. M., & Caux, E. 2001, *A&A*, 376, 1064
- Zhou, S. et al. 1993, *ApJ*, 419, 190

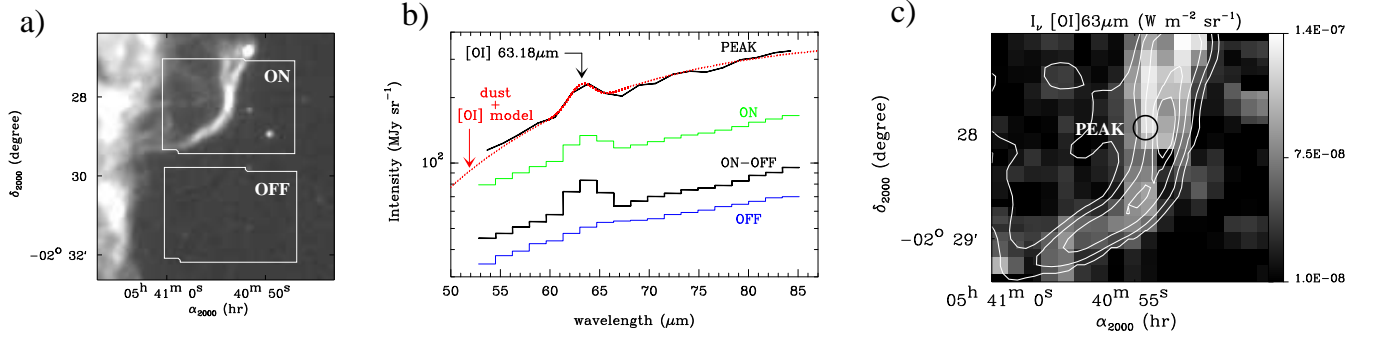


Fig. 1.— (a) ISOCAM ($5\text{--}8.5\mu\text{m}$) image of the Horsehead (dominated by PAH emission; Abergel et al. 2003). The ON- and OFF-source areas of our *Spitzer*/MIPS observations are shown. (b) Different spectra: mean ON-source (green histogram), OFF-source (blue histogram), and ON-OFF (black histogram). The MIPS spectrum toward the PDR (PEAK position) is shown on top (black continuous curve) together with our dust and [O I] radiative transfer model convolved with MIPS/SED spectral resolution. (c) [O I] $63\mu\text{m}$ intensity map. The scale is shown in the look-up table (in $\text{W m}^{-2} \text{sr}^{-1}$). The white contours represent the *ortho*- H_2 $v=0\text{--}0$ $S(1)$ line intensity at $\sim 17\mu\text{m}$ ($0.9\times$, $1.5\times$, $2.5\times$, $3.5\times$, and $4.0\times 10^{-8} \text{W m}^{-2} \text{sr}^{-1}$; Habart et al. 2009). The circle represents the $\sim 15''$ -FWHM resolution toward the PEAK.

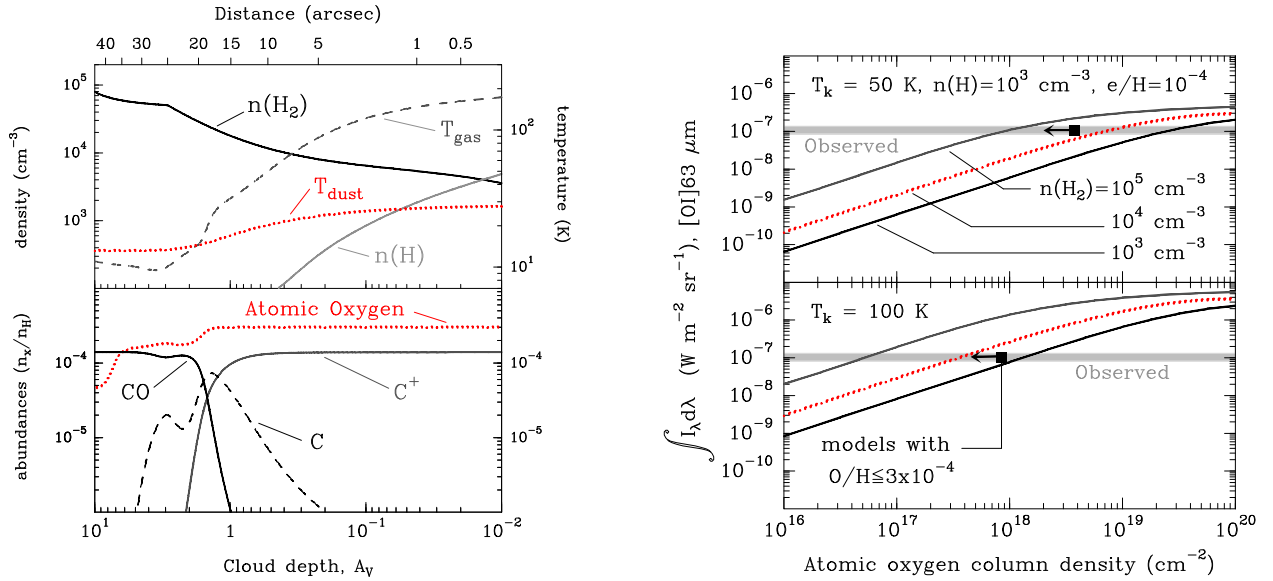


Fig. 2.— *Left*: PDR model adapted to the Horsehead ($G_0=100$ and density gradient from Goicoechea et al. 2009). The upper panel shows the resulting H_2 and H density profiles, together with the T_k and T_d temperature gradients. The lower panel shows the $\text{CO}/\text{C}/\text{C}^+$ transition and the predicted abundance profile of atomic oxygen. *Right*: output of a grid of *nonlocal*, non-LTE radiative transfer models. Panels show the expected $[\text{O I}]63 \mu\text{m}$ line intensity (in $\text{W m}^{-2} \text{sr}^{-1}$) as a function of $N(\text{O I})$ for two gas temperatures ($T_k=50$ and 100 K) and different gas densities: $n(\text{H})=10^3 \text{ cm}^{-3}$ fixed and varying $n(\text{H}_2)$. The shaded regions show the $[\text{O I}]63 \mu\text{m}$ line intensity observed by *Spitzer*/*MIPS* toward the PEAK.